Ice-melt rates during volcanic eruptions within water-drained, low pressure subglacial cavities

D C Woodcock, S J Lane and J S Gilbert

Lancaster Environment Centre, Lancaster University, Lancaster LA1 4YQ, UK

d.woodcock@lancaster.ac.uk

Abstract

Subglacial volcanism generates proximal and distal hazards including large-scale flooding and increased levels of explosivity. Direct observation of subglacial volcanic processes is infeasible; therefore, we model heat transfer mechanisms during subglacial eruptions under conditions where cavities have become depressurized by connection to the atmosphere. We consider basaltic eruptions in a water-drained, low pressure subglacial cavity, including the case when an eruption jet develops. Such drained cavities may develop on sloping terrain, where ice may be relatively shallow and where gravity drainage of meltwater will be promoted. We quantify, for the first time, the heat fluxes to the ice cavity surface that result from steam condensation during free convection at atmospheric pressure and from direct and indirect radiative heat transfer from an eruption jet. Our calculations indicate that the direct radiative heat flux from a lava fountain (a "dry" end-member eruption jet) to ice is c. 25 kW m^{-2} and is a minor component. The dominant heat transfer mechanism involves free convection of steam within the cavity; we estimate the resulting condensation heat flux to be c. 250 kW m^{-2}. Absorption of radiation from a lava fountain by steam enhances convection but the increase in condensing heat flux is modest at c. 25 kW m^{-2}. Overall, heat fluxes to the ice cavity surface are likely to be no greater than c. 300

kW m^{-2}. These are comparable with heat fluxes obtained by single phase convection of water in a subglacial cavity, but much less than those obtained by two-phase convection.

1. Introduction

Subglacial eruptions where magma has fragmented by explosion or granulation are often characterized by the rapid release of large quantities of meltwater and, on many occasions, by penetration of the overlying ice sheet or glacier ice to become subaerial [*Gudmundsson*, 2005]. Rapid release of meltwater has the potential to damage infrastructure in its path. In addition, the meltwater flow may mobilize volcanic sediments to generate lahars with potential for both infrastructure damage and loss of life [*Major and Newhall*, 1989].

We consider a subglacial fissure eruption in which a connection to the atmosphere becomes established and where two conditions are met: (1) meltwater drains from the cavity to allow the development of a vapor-dominated cavity; drainage will be promoted by steep terrain and/or large diameter meltwater conduits, and (2) the cavity persists in the face of ductile ice flow that will tend to collapse the cavity; a condition favored by thin ice, cold (strong) ice and rapid melt back of the cavity walls. We discuss this second condition further in Section 5.4. Under these conditions cavity pressure is low (i.e. near atmospheric), thus explosive activity may be enhanced and an eruption jet of pyroclasts with varying amounts of steam may develop in the subglacial cavity. *Magnússon et al.* [2012] describe the development of a minor eruption on slopes south of the summit caldera of Eyjafjallajökull, where the terrain was steeper and the ice thinner than at the summit region. Figure 4d in *Magnússon et al.* [2012] shows the appearance of a new cauldron that was not present in the corresponding image taken 38 s earlier. This earlier image shows a supraglacial meltwater channel starting some 300 m downslope from where the new cauldron later appears. A pair of images taken approximately an hour earlier shows no sign of this

meltwater channel. *Magnússon et al.* [2012] suggest that the subglacial phase of this minor eruption was liquid-dominated initially but subsequently drained meltwater.

For basaltic magmas, *Wilson et al.* [2013] proposed that a water-drained, low pressure subglacial cavity may be produced if a subglacial sill, growing outwards from a feeder dyke, reaches the edge of the enclosing ice body. Drainage of meltwater from the top of the sill is considered to be sufficiently rapid to allow the top of the sill to depressurize and undergo explosive fragmentation. Depressurization propagates backwards towards the vent, initiating a Hawaiian-style lava fountain that "drills" through the overlying ice by pyroclast impact up to the unconstrained height of the fountain. Melting of the cavity then continues by radiative heat transfer from the lava fountain [*Wilson et al.,* 2013].

Figure 1 shows a schematic diagram of a water-drained, low pressure ice cavity formed during a subglacial fissure eruption and containing an eruption jet. In this scenario, we expect the cavity fluid to be at or slightly above atmospheric pressure with the connection to the atmosphere maintained by the flow of hot meltwater or steam from the cavity to the edge of the enclosing ice body. The nature of the eruption jet will depend on the degree of magma-water interaction within the shallow volcanic conduit. For minimal interaction between water and basaltic magma a lava fountain may become established. As the extent of magma-water interaction increases, a lava fountain is progressively transformed to an ash-laden steam jet. This behavior is well illustrated around 5 minutes into a video clip of the 1959-1960 Kilauea eruption [*YouTube*, 2007], where the magma intermittently contacts shallow groundwater. The cavity fluid is expected to comprise mainly steam (water vapor),

sourced from magmatic gas and phreatomagmatic activity. For the "dry" end-member case of a lava fountain we envisage that much of the phreatomagmatic steam is produced by contact of the meltwater rain from the cavity roof onto short clastogenic lava flows on either side of the lava fountain and by the interaction of hot spatter with water on the floor of the cavity. The spatter may fragment, cool rapidly and generate copious amounts of steam. Any steam generated that is not condensed within the cavity may be vented out of the cavity. The presence of an eruption jet is, however, not necessary for heat transfer from magma to ice within the cavity. Hot lava or hot pyroclasts proximal to the vent will drive a free convective circulation that comprises an ascending limb of steam over the vent together with a descending limb of steam and water droplets adjacent to the cavity walls, where condensation of steam occurs. We show in Section 3 that steam condensation is the primary heat transfer mechanism in water-drained low pressure subglacial eruption cavities.

In this paper we quantify ice-melt rates during volcanic eruptions within low pressure subglacial drained cavities and compare the results with other subglacial eruption scenarios, specifically where the subglacial eruption cavity is filled with liquid water or steam at or near glaciostatic pressure [*Woodcock et al.,* 2014, 2015]. In particular we consider (1) direct radiative transfer from the surface of pyroclasts in the outer envelope of an eruption jet to the walls and roof of the ice cavity, (2) steam condensation that occurs during free convection within the cavity, and (3) the possibility that convection may be enhanced by absorption of radiation from the jet by the steam in the cavity. In particular we attempt, for the first time, to quantify heat transfer rates within an idealized model system using published heat transfer methods to estimate likely heat fluxes.

2. Direct radiative heat transfer

In this section we estimate the heat transfer rate by direct radiative heat transfer between a linear dyke-fed eruption jet and an overlying ice cavity that is drained and vented to atmospheric pressure. We develop a first order conceptual model of the system to estimate the heat flux on the ice cavity surface. We focus on lava fountains here because they are likely to have the highest radiative heat flux.

2.1. Conceptual model

Figure 2 shows the conceptual model used for the radiation calculations. For expediency, we assume an ice cavity at atmospheric pressure that is triangular in cross section within which a lava fountain extends to the cavity roof. Both the cavity and the lava fountain extend along a linear eruption fissure that is long compared to the height of the cavity. We model the lava fountain as a vertical planar surface that radiates in all directions (i.e. as a "diffuse" or "Lambert" surface). The emissivity of lava approaches unity [*Pinkerton et al*., 2002], so the lava fountain surface can be considered as a black body.

The assumption of a complete wall of lava ("curtain of fire") without gaps overestimates the radiative heat flux, but may be reasonable for the early stages of a Hawaiian-style fissure eruption. As the eruption progresses, activity often becomes localized to discrete locations along the vent [*Vergniolle and Mangan*, 2000]. For the analysis of this situation a model with axisymmetric symmetry may be more appropriate.

129 The direct radiative heat flux from the lava fountain has a strong dependence on the
130 temperature of pyroclast surfaces that can "see" the ice surface. *Davies et al.* [2011]
131 measured temperatures of up to 1140 °C during thermal infrared (FLIR) observations
132 of small (2-3 m high) lava fountains from the Erta' Ale lava lake, although this
133 temperature must be regarded as an extreme case. For larger lava fountains the heat
134 lost from pyroclasts by radiation and forced convection as pyroclasts travel through
135 the fountain may be considerable; thus FLIR-determined temperatures of lava
136 fountains are generally much lower than those measured at Erta' Ale. For example,
137 *Spampinato et al.* [2008] recorded lava fountain temperatures of around 700 °C during
138 the Etna 2002-3 fissure eruption for fountains 100-300 m high erupting along a 1 km
139 fissure. Within the "wet" environment of a subglacial cavity, lava fountain
140 temperatures may be reduced further by magma-water interaction.
141
142 Although clear ice is transparent to visible radiation it is almost opaque to infra-red
143 radiation [*Brandl and Warren*, 1993]. Black body radiation at 700 °C has a peak
144 energy wavelength λ_{max} of around 3 μm, with more than 99% of the radiative energy
145 at wavelengths longer than 1 μm [*Incropera and DeWitt*, 1996]. *Hobbs* [1974]
146 tabulates data on the wavelength-dependent absorption coefficient for ice; these data
147 show that most of the radiation emitted by the lava fountain will be absorbed in the
148 first millimetre below the surface of the ice. Accordingly, we model the ice surface as
149 a black body at 0 °C.
150
151 The base of the cavity may comprise a layer of wet rock or pools of meltwater. The
152 water will absorb radiation from the lava fountain, but cannot attain a temperature

153 greater than 100 °C, the boiling point of water at 0.1 MPa. The cavity base will
154 reradiate to the ice cavity, but the radiative flux will be small and is neglected.
155
156 The gas in the cavity will comprise a mixture of air and steam at atmospheric pressure.
157 Dry air is almost transparent to infra-red radiation while steam absorbs infra-red
158 radiation to some degree. The presence of steam in the cavity will reduce the radiative
159 flux from the lava fountain to the ice cavity because the steam will absorb some of the
160 radiation from the lava fountain and re-radiate it at a lower temperature. In section 2.2
161 we assume that there is no absorbing medium in the cavity and that the lava fountain
162 surface can exchange radiation directly with the ice cavity surface. The resulting heat
163 flux is thus an upper bound on the likely radiative heat flux.
164
165
166 **2.2. Radiative heat transfer between surfaces**
167 In the absence of an absorbing medium in the cavity, radiation exchange between
168 surfaces depends on the geometry and orientation of the surfaces as well as the
169 radiation properties and temperatures of the surfaces. Geometry and orientation are
170 accounted for by defining a "view factor", F_{ij}, which is the fraction of the radiation
171 leaving surface *i* that is intercepted by surface *j*. In general, the evaluation of view
172 factors is complex; however Hottel's "crossed string" method [*Hottel and Sarofim,*
173 1967] can be used for surfaces that are long in one direction.
174
175 The net power radiated per unit length from one side of the lava fountain to one half
176 of the ice surface (both considered to be black bodies) is given by *Incropera and*
177 *DeWitt* [1996]:

178 $$E = \sigma A F (T_L^4 - T_i^4) \qquad (1)$$

179 where σ is the Stefan-Boltzmann constant (5.67×10^{-8} W m^{-2} K^{-4}), A is the area of the
180 lava fountain (= H m^2 m^{-1}), T_L and T_i are the lava and ice absolute temperatures and F
181 is the view factor of the ice surface from the lava fountain (= $1/\sqrt{2}$, see Appendix A).
182 The surface of the ice exposed to radiation is $H\sqrt{2}$ m^2 m^{-1}. The heat flux on the ice
183 surface is thus given by:

184 $$Q = \frac{\sigma (T_L^4 - T_i^4)}{2} \qquad (2)$$

185 For a lava fountain with a mean effective surface temperature of 700 °C, the resulting
186 heat flux is 25 kW m^{-2}. Direct radiative heat fluxes thus appear to be much smaller
187 than some of the heat fluxes calculated for convective heat transfer in both flooded
188 and drained cavities [*Woodcock et al.,* 2014; 2015], where heat fluxes of up to 5 MW
189 m^{-2} are plausible. We conclude that direct radiative heat transfer is likely to be a
190 minor ice melting mechanism within drained, low pressure subglacial eruption
191 cavities.
192

193 **3. Steam condensation heat transfer from free convection**

194 **3.1 Introduction**

195 In this section, we develop a model for the convection of saturated steam within a
196 roofed cavity in the absence of an eruption jet. We consider the effect of an eruption
197 jet on the convection in Section 4. Condensation is the principal mechanism of heat
198 transfer from the circulating steam to the sloping ice cavity roof. The heat flux may
199 be evaluated using the method used in *Woodcock et al.* [2015], given a value for the
200 convective circulation velocity.
201

202 The condensate and meltwater produced on the ice surface is envisaged to drip from
203 the ice cavity roof in a rain of droplets. The presence of these droplets drives the
204 circulation by density increase and by transferring momentum to the circulation.
205
206 **3.2. Model development**
207 Figure 3 shows the elements of the model for the circulation within a prismatic cavity
208 of triangular cross-section with a height H and a basal half-width bH. The triangular
209 shape is chosen for expediency but the model could be generalised for other
210 geometries. The circulation comprises an upward flow of steam parallel to the cavity
211 center line, followed by a return downward flow along the sloping roof of the cavity
212 (where heat transfer melts ice) followed by a horizontal flow to complete the loop.
213 The flow is assumed to be confined to a channel of width kH ($k < 0.5$) that is constant
214 for the whole of the circulation. As a starting point, we assume a constant volume
215 drained cavity, where melt rates are matched to ductile ice creep rates.
216
217 ***3.2.1 Driving force for circulation***
218 The presence of the droplets in the downward flow increases the density and thus
219 contributes to the pressure difference that drives convection. This "droplet density"
220 ρ_{dr} is given by:

221 $$\rho_{dr} = \frac{m_{cmw}}{u_t} \qquad (3)$$

222 where m_{cmw} is the flux of condensate and meltwater in the droplet rain and u_t is the
223 average droplet terminal velocity (Appendix B). The resulting pressure difference is
224 thus $\rho_{dr}\, gH$.
225

The motion of the droplets also contributes to the pressure difference that drives convection. As droplets fall, they experience a drag force that is equal to their weight. An equal and opposite force acts on the surrounding steam and this force has a component in the steam flow direction parallel to the cavity roof. The resulting effect, expressed as a pressure, is given by $\rho_{dr}\, gH$. The overall "driving" pressure difference is thus

$$\Delta P_{dr} = 2gH\rho_{dr} \qquad (4).$$

3.2.2 Overall circulation flow

The momentum balance over an element of the flow with height dh, density ρ, velocity u, and pressure P is:

$$dP = \rho g dh + 0.5\rho u^2 dK + \rho u du \qquad (5)$$

where the three terms on the right hand side are the "gravitational," "frictional," and "accelerational" pressure changes, respectively and dK is the loss coefficient [*Massey*, 1970].

For the circulation loop within the cavity the net pressure and velocity changes are zero and the mass flowrate per unit area ρu is constant. Thus Equation (5) can be integrated around the circulation loop to give:

$$g\int \rho \,\mathrm{dh} + 1/2 \int \rho u^2 dK = 0 \qquad (6).$$

The first term comprises the net pressure difference that drives the convective circulation flow. This "driving" pressure difference is balanced by the second term: the pressure loss due to friction and change of direction within the circulation loop. An expression for this "resisting" pressure difference ΔP_{res} can be developed by adapting the expression in *Woodcock et al.* [2014]; thus

$$\Delta P_{res} = 0.5\left(\frac{m}{kH}\right)^2 \times \left(\frac{K_1}{\rho_1} + \frac{K_2}{\rho_2}\right) \qquad (7)$$

where K_1 and K_2 are the loss coefficients for the bends in the circulation loop, and ρ_1 and ρ_2 are the densities at the top and bottom of the upward flow respectively.

The circulation flowrate can be determined by equating the driving and resisting pressure differences:

$$m = 2kH\left[\frac{gH\rho_{dr}}{K_1/\rho_1 + K_2/\rho_2}\right]^{0.5} \qquad (8).$$

The circulation velocity is used to update the value of the condensing heat flux and Equation (8) is re-evaluated to convergence. Fortunately, for the range of circulation velocities encountered, the heat flux is relatively insensitive to velocity, so satisfactory convergence can be obtained within one or two iterations.

3.3. Results

We evaluate Equation (8) using the same conditions as the reference case in Table 1. The resulting mass flowrate per unit length of cavity is 13.5 kg s^{-1} m^{-1}; the corresponding condensing heat flux is 186 kW m^{-2}. There is thus significant heat transfer by free convection within the cavity, independent of the presence of an eruption jet.

4. Enhancement of free convection by radiative heat transfer

4.1 Introduction

In this section we establish the extent to which the presence of an eruption jet enhances the circulation. We consider absorption of radiation by the steam adjacent to the eruption jet within a roofed cavity during a subglacial eruption. The consequent temperature increase and reduction in density as the steam is superheated will provide

additional driving force and enhance the free convection. In section 4.2, we develop a model for this mechanism in order to estimate the likely melting heat flux.

Studies of free convection in vertical channels have been reported in the literature. *Cheng and Muller* [1998] and *Li et al.* [2013] carried out numerical studies of free convection of air in vertical channels where one plane wall was heated and the opposite wall was unheated apart from radiative heat transfer across the channel. In both studies the air was assumed to be radiatively transparent and any changes in air temperature to occur by convective heat transfer from the vertical walls. The situation considered by *Cheng and Muller* [1998] and *Li et al.* [2013] is not the situation that we envisage, where steam can absorb radiation. However, we are not aware of any study in which a freely convecting fluid is heated by absorption of thermal radiation.

The absorption of a collimated beam of monochromatic radiation may be modelled by the Beer-Lambert law [*Incropera and DeWitt,* 1996]:

$$dI = -\kappa I dz \qquad (9)$$

where dI is the amount of radiation absorbed from a beam with an incident radiative flux (I) over a thickness dz and κ is the attenuation coefficient. If κ is constant through a finite thickness L, Equation (9) may be integrated to give:

$$\left(\frac{I}{I_o}\right) = e^{-\kappa L} \qquad (10)$$

where I_o is the incident radiative flux on the gas layer of thickness L (known as the "beam length") and I is the flux emerging from the layer.

For absorption of radiation by a gas, Equation (10) may be written as

299 $$\ln\left(\frac{I}{I_o}\right) = -\phi pL \qquad (11)$$

300 where p is the partial pressure of the absorbing gas in the layer and φ is the absorption
301 coefficient. The product pL is known as the optical depth. The absorption coefficient
302 for a given waveband in general depends on temperature and total pressure.
303
304 A hot surface such as the surface of a lava fountain emits a continuous spectrum of
305 radiation. In order to evaluate the total radiation absorbed by the gas one needs to
306 evaluate the absorption for each increment of waveband and integrate over the whole
307 spectrum. Hottel [*Hottel and Sarofim*, 1967] tackled this problem by considering the
308 emission of radiation from an isothermal hemisphere of gas to a surface element at the
309 centre of its bounding diameter. Hottel defined a "standard emissivity" ε_g as the ratio
310 of the radiation from the gas hemisphere to the radiation from a hemispherical black
311 body shell with the same diameter and at the same temperature. Values of standard
312 emissivities, which depend on the nature and optical depth of the absorbing gas,
313 together with the gas temperature and total pressure, are summarised in *Hottel and*
314 *Sarofim* [1967].
315
316 The values of standard emissivity relate to a hemispherical volume of gas. Hottel
317 enabled his results to be extended to other geometries by his concept of "mean beam
318 length" (L_e): the radius of a hemisphere of gas for which the emissivity is the same as
319 the volume of gas under consideration [*Hottel and Sarofim,* 1967]. Tables of mean
320 beam length for a number of geometries, together with Hottel's charts of standard
321 emissivity, are widely used in the engineering solution of radiative heat transfer
322 problems [*Hottel and Sarofim,* 1967, *Incropera and DeWitt,* 1996].

Finally, *Hottel and Sarofim* [1967] showed that the absorbtivity α_g of a gas, at temperature T_g, that absorbs radiation from a black body with a surface at temperature T_s should be given by

$$\alpha_g = \varepsilon_g \left(\frac{T_g}{T_s} \right)^{0.5} \qquad (12)$$

where ε_g is the gas emissivity evaluated at T_s and for a modified mean beam length of L_e (T_s / T_g). In practice, an exponent on the temperature ratio of 0.45 provides a better fit to experimental data [*Incropera and DeWitt,* 1996].

4.2 Model development

4.2.1 Upward flow

Consider an element of unit length with a vertical thickness *dh* at height *h* above the base of the model cavity in the upward flow. We assume that any horizontal variation in steam temperature in an element is eliminated by turbulence, thus the steam temperature can be defined by $T_g(h)$. The net radiative heat transfer rate per unit length *dq* into the steam flow through this element is:

$$dq = \sigma(\alpha_g T_L^4 - 2\varepsilon_g T_g^4) dh \qquad (13)$$

where σ is the Stefan-Boltzmann constant, T_L is the temperature of the lava fountain surface (assumed independent of *h*), α_g and ε_g are the absorptivity and emissivity of the steam at height *h*. The factor of 2 arises because the steam flow emits radiation in both directions. The net radiative heat transfer raises the temperature of the steam by dT_g :

$$dq = mC_p dT_g \qquad (14)$$

where m is the steam mass flowrate per unit length with specific heat capacity C_p. Equations (13) and (14) may be combined to produce an equation for the rate of change of steam temperature with height within the upward flow:

$$\frac{dT_g}{dh} = \frac{\sigma(\alpha_g T_L^4 - \varepsilon_g T_g^4)}{mC_p} \qquad (15).$$

For steam at 0.1 MPa, emissivities are almost independent of temperature at long optical depths over the temperature range 373 – 900 K [*Incropera and DeWitt*, 1996]. The dependency of emissivity on optical depth pL can be represented by the equation

$$\varepsilon_g = 0.6 - 0.087 \ln\left(\frac{6.1}{pL}\right) \quad \text{with } 0 \le \varepsilon_g \le 1 \quad (16)$$

where the mean beam length for this geometry is equal to 1.8 kH [*Incropera and DeWitt*, 1996]. The absorptivity for steam at 0.1 MPa is given by

$$\alpha_g = \varepsilon_g \left(\frac{T_g}{T_L}\right)^{0.45} \qquad (17)$$

where ε_g is evaluated at T_L for the modified optical depth of $pL\ (T_L / T_g)$.

Equation (15) cannot be solved analytically, but may be solved by numerical methods. The temperature rise ΔT_g over an element of finite vertical width ΔH is given by

$$\Delta T_g = \frac{\Delta H \sigma(\alpha_g T_L^4 - \varepsilon_g T_g^4)}{mC_p} \qquad (18).$$

The steam temperature, and thus the steam density, can be determined for each element for any circulation rate. The pressure difference over element i due to the weight of the steam with density ρ_i is

$$\Delta P_i = \rho_i g \Delta H \qquad (19).$$

The corresponding pressure difference for the whole upward flow is thus

$$\Delta P_r = g\Delta H \Sigma \rho_i \qquad (20).$$

The pressure difference between the top and base of the cavity is of order 10^3 Pa compared with the total pressure of 10^5 Pa; density differences due to changes in pressure may thus be neglected.

4.2.2 Downward flow

Within the downward flow, the principal mechanism for heat transfer from the circulating steam to the ice surface is condensation. The passage of condensate and meltwater droplets through the vertical width of the downward flow cools the circulating steam further by convection and radiation to the droplet surfaces (Appendix B). In addition, heat is transferred from the hot steam to the ice surface by radiation, although this is only significant at high steam temperatures.

If the total heat removal rate per unit length is Δq for an element ΔH of the downward flow, the corresponding temperature decrease ΔT_g is given by:

$$\Delta T_g = \frac{\Delta q}{m C_p} \qquad (21).$$

Equation (21) is valid provided that the steam temperature is greater than the local boiling point; below the saturation level in the downward flow the temperature is then constant. The steam density for each element can then be evaluated once the various contributions to Δq have been calculated.

The pressure difference for the downward flow is thus

$$\Delta P_d = g\Delta H (\Sigma \rho_i + \Sigma \rho_{dr}) \qquad (22)$$

where ρ_i comprises the sum of the steam density and the droplet density (Section 3.2.1). The net pressure difference that drives the convective circulation flow is given by

$$\Delta P_{dr} = \Delta P_d - \Delta P_r \qquad (23).$$

This "driving" pressure difference is balanced by the pressure loss due to friction and change of direction within the circulation loop. An expression for this "resisting" pressure difference ΔP_{res} is given by Equation (7) in Section 3.2.2.

The equations that describe the fluid flow and heat transfer have been set up as a spreadsheet in Excel. The circulation flow rate that occurs when the driving and resisting pressure differences are equal can be found using the Goal Seek option. The resulting circulation velocities and temperatures are used to determine the heat flux from steam condensation; thus both the circulation flow model and the steam condensation model need to be converged simultaneously.

4.3. Results

Table 1 shows the results of a "reference case" calculation, together with a number of sensitivity studies to illustrate the effect of varying cavity height, aspect ratio, flow width and loss coefficients together with the effect of changing eruption jet surface temperature and cavity pressure. Case 7, with an eruption jet surface temperature set to 370 K, has results that are identical to those calculated in Section 3.3 for free convection of steam in the absence of an eruption jet.

Our mechanism requires the generation of steam as well as radiative heat from the eruption jet. Steam generation will require some degree of phreatomagmatic

416 interaction within the shallow volcanic conduit or in the cavity, although the degree of
417 interaction may vary significantly in time and space. Figure 1 shows the case where
418 steam production occurs on either side of the eruption jet by contact of the "rain" of
419 condensate from the roof onto hot volcanic deposits. For the reference case we have
420 chosen a temperature of 973 K for the eruption jet surface temperature. Increasing
421 degrees of phreatomagmatic interaction will result in a colder eruption jet: we explore
422 this with a "step out" case in Table 1.
423
424 Three general conclusions can be drawn from the results presented in Table 1. Firstly,
425 steam temperatures are relatively low, precluding significant heat transfer by radiation
426 from the steam. Thus, in the downward flow, heat transfer is dominated by
427 condensation. Secondly, the circulation velocities are sufficiently fast that heat flux is
428 relatively insensitive to velocity (Figure 4). Thirdly, for the same conditions, the
429 radiative enhancement of heat flux (an additional 25 kW m^{-2} for the reference case
430 conditions) is relatively modest. All heat fluxes are much smaller than heat fluxes
431 calculated for convective heat transfer in both flooded and drained cavities [*Woodcock*
432 *et al.,* 2014; 2015]. The effect of individual variables is discussed below.
433
434 *(i) Variation in cavity height H (compare case 2 with reference case)*
435 Doubling cavity height potentially doubles the driving ΔP, while the resisting ΔP is
436 proportional to $(m/kH)^2$ via Equation (7). Thus circulation rate m might be expected to
437 increase by $2^{3/2}$ or 2.8; this is close to the determined increase.
438
439 *(ii) Variation in cavity aspect ratio b (compare case 3 with reference case)*
440 Increasing aspect ratio should increase circulation rate because desuperheating of the
441 downward flow is completed at a greater height, so the driving force for circulation is

increased. The effect is small because the length of cavity wall needed for desuperheating is short and most of the downward flow comprises saturated steam.

(iii) Variation in flow width (compare case 4 with reference case)

Circulation rate is expected to increase linearly with flow width (at constant H). The observed increase is slightly less because the temperature increase in the upward flow decreases slightly, thus reducing the driving force for circulation.

(iv) Variation in bend K value (compare case 5 with reference case)

Doubling the K values should reduce the circulation rate by a factor of $2^{1/2}$. However a reduced circulation rate allows a larger temperature rise in the upward flow, slightly increasing the driving force for circulation.

(v) Variation in eruption jet temperature (compare case 6 and 7 with reference case)

Changes in eruption jet temperature appear to have little effect on heat flux. There are two reasons for this. Firstly, provided that the circulation velocity is sufficiently fast, the condensing heat flux is relatively insensitive to velocity. Secondly, the circulation has two drivers. One driver is the density difference produced by the temperature difference between the upward and downward flows – this depends on the amount of radiation absorbed by the upward flow, which in turn depends on the temperature of the eruption jet. The second driver is the presence of liquid droplets in the downward flow – this increases the density difference between the upward and downward flow and transfers momentum into the downward flow (section 3.2.1). This second driver is largely independent of eruption jet temperature; it depends only on sufficient steam

being available and the convection being "focused" with the upflow over the vent and downflow along the ice cavity walls.

(vi) Variation in cavity pressure (compare case 8 with reference case)

Doubling the cavity pressure increases steam absorptivity by around 20% [*Incropera and DeWitt,* 1996] and doubles the density for a given temperature. The net effect is that the temperature rise in the upward flow is almost unchanged. In the downward flow, droplet density is increased due to reduced terminal velocity: this increases the driving force for circulation. The net effect is to increase the overall driving force for circulation by $2^{1/2}$, but this is balanced by a frictional pressure drop that is inversely proportional to steam density via Equation (7). The resulting circulation rate is thus expected to increase by a factor of around $2^{3/4}$ (1.7), similar to the observed increase.

5 Discussion

5.1 Concentration of non-condensable gases in the cavity

The condensation heat flux depends on the concentration of non-condensable gases in the cavity. The reference case value of 0.1 mole fraction is justified as follows. The sources of non-condensable gases in a subglacial eruption cavity were reviewed by *Woodcock et al*. [2015]. They include air from melted ice (c. 0.5 kg/tonne magma) and the non-condensable gases, principally CO_2, exsolved from magma. The total magmatic gas exsolved is around 10 kg/tonne magma, of which c. 15% is non-condensable. The cavity is an open system that is vented at atmospheric pressure: the non-condensable gas concentration would thus be (0.5 +1.5)/10.5 or 0.19 mass fraction (equivalent to 0.14 mole fraction). The rate of steam generation from magma-water interaction, together with magmatic steam, is likely to be in excess of

492 the steam condensation rate. The excess steam will thus dilute the non-condensable
493 gases.
494
495 We explore the sensitivity to non-condensable gas mole fraction for the reference case
496 cavity pressure and dimensions. Figure 5 shows two curves for condensation heat flux
497 versus non-condensable mole fraction: one curve assumes that the non-condensable
498 component is air; the other assumes it to be CO_2, but with its radiative properties
499 modeled by steam for expediency. The principal effect of increasing the non-
500 condensable mole fraction is to reduce the condensation heat flux, as demonstrated in
501 *Woodcock et al.* [2015]. Additional minor effects that arise from the nature of the
502 non-condensable component are changes in gas density, gas absorptivity and gas
503 specific heat capacity. If the non-condensable component is radiatively transparent
504 then the absorptivity of the gas mixture in the upward flow decreases with increase in
505 non-condensable mole fraction.
506
507 For comparison, Figure 5 also includes the direct radiation heat flux evaluated in
508 Section 2.2. The zero-steam value of 25 kW m^{-2} assumes that the cavity gases are
509 radiatively transparent. As the proportion of steam increases, the direct radiation heat
510 flux decreases because some of the radiation from the eruption jet is absorbed by the
511 steam and re-radiated at a cooler temperature. In the reference case, the absorbtivity
512 of the cavity gases is c. 0.3; a lower bound on the direct radiation flux is thus 25(1-
513 0.3) i.e. c. 18 kW m^{-2}.
514
515 ***5.2. Liquid film thinning by gas shear***

516 The condensing heat fluxes reported in Section 4.3 neglect any effects due to thinning
517 of the liquid film of meltwater and condensate by the co-current flow of steam. The
518 effect of tangential shear on the liquid film thickness and thus on the condensing heat
519 flux was studied by *Rohsenow et al.* [1956]. They showed that, for laminar films, the
520 "no-shear" heat transfer coefficient should be increased by a factor of $[1 + (4U \tau_g / 3g$
521 $\sin\theta \rho_w k_l)]$, where τ_g is the tangential shear stress at the liquid film surface, U is the
522 film heat transfer coefficient, θ is the inclination of the surface from the horizontal and
523 k_l is the liquid thermal conductivity. The ratio k_l / U may be replaced by the film
524 thickness δ, whence the factor becomes $[1 + (4 \tau_g / 3g \sin\theta \delta \rho_w)]$, where the second
525 term is approximately the ratio of the shear force to the gravitational force on the
526 liquid film [*Rohsenow et al.,* 1956].
527
528 *Rohsenow et al.* [1956] extended their analysis to include turbulent liquid films and
529 provided a method for evaluating τ_g. Application of their results to the reference case
530 in Table 1 shows that tangential shear increases the heat flux by around 30%.
531
532 ***5.3. Comparison with inferred fluxes from recent eruptions***
533 In Section 2 we showed that an upper bound on direct radiative heat flux is
534 approximately 25 kW m^{-2}. Table 1 indicates condensing heat fluxes from radiatively
535 enhanced free convection of 200-300 kW m^{-2}; these should be increased by 30% to
536 account for tangential shear. Figure 4 indicates that any forcing of the convection by
537 momentum transfer from the eruption jet is unlikely to increase heat fluxes
538 significantly. Overall, heat fluxes from lava to ice cavity surface are likely to be no
539 greater than 300-400 kW m^{-2}. These are similar to those calculated by *Woodcock et*
540 *al*. [2014] for single phase convection in liquid-filled cavities.

Heat fluxes of 300-400 kW m^{-2} will melt ice with a vertical penetration rate of around 3-5 m h^{-1} if meltwater leaves the ice cavity surface at 0 °C. The assumption of meltwater at 0 °C is unrealistic but provides an upper bound on penetration rate. The rate is approximately halved for a meltwater temperature approaching the boiling point. These ice penetration rates may be compared with rates of 16 and 50 m h^{-1} inferred for the Gjálp 1996 eruption [*Gudmundsson et al.,* 2004] and the 2010 Eyjafjallajökull summit caldera eruption [*Magnússon et al.,* 2012] respectively. In both of these cases much of the evidence suggests that the subglacial cavities were predominantly liquid water-filled.

5.4. The effect of ductile ice flow

In the Introduction we mentioned that an eruption jet can only occur during subglacial eruptions if a cavity can persist in the face of ductile ice flow that will tend to collapse the cavity. *Tuffen* [2007] indicates that, for a hemicylindrical cavity, the relative rate of cavity closure by ductile ice deformation is given by:

$$\frac{1}{R}\frac{dR}{dt} = (\Delta P_a / nB)^n \qquad (24)$$

where R is the cavity radius, ΔP_a is the cavity underpressure (glaciostatic pressure in our case), B is the ice deformation parameter (a measure of ice strength) and n has a value of 3.

For a given ice thickness, a cavity developed in ice of a given strength can only be sustained in the face of ductile collapse if the melt back rate is sufficiently high. *Tuffen* [2007] explores this behavior and shows that explosive magmatism can only be sustained, for the Gjálp 1996 eruption rate, for cavity underpressures below 4 MPa (i.e

566 < 400 m ice) in ice at 0° C. In Section 5.3 we show that melt back rates are much
567 lower than those inferred for the Gjálp 1996 eruption. This example illustrates that
568 thin ice is a necessary condition for explosive activity within drained, low pressure
569 subglacial cavities in temperate glaciers.
570
571 ***5.5. Overall mass and heat balance***
572 Figure 6 shows the overall mass and heat balance for the convection system within the
573 ice cavity for the reference case in Table 1. Of the 16.5 kg s^{-1} steam circulation per
574 meter length of fissure, 10.5 kg s^{-1} m^{-1} condenses on the ice cavity roof, liberating heat
575 at a rate of 23590 kW m^{-1} and producing 31.3 kg s^{-1} m^{-1} meltwater (at 370 K). The
576 steam condensed is replenished by the evaporation of 10.5 kg s^{-1} m^{-1} condensate and
577 meltwater (CMW); the remaining CMW drains from the cavity. Note that, although
578 the flows of condensing steam and the resulting condensate are shown as discrete
579 arrows on the diagram, in reality they are "diffuse" flows that occur along the width of
580 the cavity.
581
582 The radiant heat flux from the eruption jet at 700 °C is 2541 kW m^{-1}. The radiation
583 heat flow of 832 kW m^{-1} in Figure 6 is the radiation absorbed by the steam circulation
584 from the eruption jet. The remaining radiation (1709 kW m^{-1}) is absorbed by steam in
585 the rest of the cavity, by the ice roof and by the cavity floor. Ultimately, this radiation
586 generates an additional 2.3 kg s^{-1} m^{-1} of meltwater that is not included within the mass
587 flowrates in Figure 6.
588
589 The heat flowrates on Figure 6 demonstrate that much of the heat required for ice-melt
590 is provided by the latent heat of steam generated within the ice cavity. Radiative heat

591 loss from the falling pyroclasts in the eruption jet is a small proportion of their initial
592 heat content; thus much of the initial heat content of the pyroclasts is retained on
593 landing. We envisage efficient steam generation by the contact of hot pyroclasts with
594 meltwater rain from the ice cavity roof and with the wet floor of the cavity.
595
596 **6. Conclusions**
597 We have used published heat transfer calculation methods to estimate heat fluxes to an
598 ice cavity surface during subglacial fissure eruptions where shallow ice and steep
599 terrain promote gravity drainage of meltwater and allow the cavity to depressurize.
600 The principal conclusions are as follows.
601
602 (1) Free convection can develop in the cavity with an ascending limb of steam over
603 the vent together with a descending limb of steam and water droplets adjacent to the
604 cavity walls, where condensation of steam occurs. The heat flux from steam
605 condensation during free convection at atmospheric pressure is c. 250 kW m^{-2} when
606 the effect of tangential shear on the liquid film is included.
607
608 (2) For basaltic magmas, a subglacial lava fountain may develop. The direct radiative
609 heat flux from lava fountain to ice cavity surface is c. 25 kW m^{-2}. Absorption of
610 radiation by steam enhances the convective circulation but the increase in condensing
611 heat flux is modest at c. 25 kW m^{-2}. The effects of radiation are thus minor compared
612 to free convection.
613
614 (3) Overall heat fluxes within water-drained, atmospheric pressure cavities during
615 subglacial fissure eruptions are likely to be no greater than c. 300 kW m^{-2}. These are

616 similar to those calculated by *Woodcock et al.* [2014] for single phase convection in
617 liquid-filled cavities but much less than those obtained by two-phase convection
618 within a liquid-dominated cavity.
619
620
621
622 **Appendices**
623
624 **Appendix A: Hottel's "crossed string" method**
625 In general, the evaluation of view factors is complex; however Hottel's "crossed
626 string" method [*Hottel and Sarofim,* 1967] can be used for surfaces that are long in
627 one direction. Figure A1 shows the general rule (on the left hand side) and applies it
628 to the geometry of the subglacial cavity (with height H) on the right hand side.
629
630
631 **Appendix B: Heat transfer to droplets in the downward flow**
632 The surface area available for heat transfer to droplets is given by:

633 $$A_d = \frac{6\rho_{dr} kH}{d\rho_w} \qquad \text{(B1)}$$

634 where ρ_{dr} is the "droplet density" defined in Equation (3), kH is the width of the
635 circulation path, ρ_w and d are the density of liquid water and the droplet diameter
636 respectively. A_d is the droplet area per unit area of ice surface.
637
638 In turbulent flow, the terminal velocity u_t of a droplet with diameter d falling through
639 steam with density ρ_i is given by

640 $$u_t = \left(\frac{4\rho_w g d}{3\rho_i C_D} \right)^{1/2} \qquad \text{(B2)}$$

641 where C_D is the droplet drag coefficient and g is the gravitational acceleration.

642

643 The convective heat transfer coefficient (U) to the droplet surface may be calculated

644 from the Ranz and Marshall correlation [*Ranz and Marshall*, 1952]

645 $$Nu = 2 + 0.6\, Re^{1/2}\, Pr^{1/3} \qquad \text{(B3)}$$

646 where Nu is the Nusselt number ($Nu = U\, d / k_g$), Re is the Reynolds number ($Re = u_t$

647 $\rho_i\, d / \mu$), Pr is the Prandtl number ($Pr = \mu\, C_p / k_g$) and μ, C_p and k_g are the viscosity,

648 specific heat capacity and thermal conductivity of steam respectively.

649

650 Heat transfer by radiation to a droplet surface may be approximated by

651 $$Q_r = \sigma\, (\varepsilon_g\, T_g^{\,4} - T_d^{\,4}) \qquad \text{(B4)}$$

652 where Q_r is the net radiation (W per m^2 droplet area) and T_d is the droplet surface

653 temperature (assumed to be the boiling point).

Notation

A area of eruption jet per unit length, m

B ice deformation parameter, Pa $s^{-1/3}$

A_d heat transfer area of droplets per unit area of ice surface, dimensionless

b aspect ratio of cavity (ratio of basal half-width to cavity height), dimensionless

C_D droplet drag coefficient, dimensionless

C_p specific heat capacity of steam, J kg^{-1} K^{-1}

d droplet diameter, m

dh increment of vertical height in cavity, m

dI amount of radiation absorbed from a beam of radiation, W m^{-2}

dq net radiative heat transfer rate into the steam flow, W

dT_g change in steam temperature, K

dz increment of thickness of absorbing medium, m

E net power radiated per unit length of eruption jet, W m^{-1}

F view factor, dimensionless

g gravitational acceleration, m s^{-2}

H height of subglacial cavity, m

I radiative flux emerging from a gas layer of thickness L, W m^{-2}

I_o incident radiative flux on a gas layer of thickness L, W m^{-2}

k ratio of channel width to cavity height, dimensionless

k_g thermal conductivity of steam, W m^{-1} K^{-1}

k_l thermal conductivity of liquid, W m^{-1} K^{-1}

K loss coefficient for overall circulation, dimensionless

K_1 loss coefficient for top bend in the circulation loop, dimensionless

K_2 loss coefficient for bottom bends in the circulation loop, dimensionless

679 L finite thickness of absorbing medium, m

680 L_e mean beam length, m

681 m steam mass flowrate per unit length, kg s^{-1} m^{-1}

682 m_{cmw} flux of condensate and meltwater in the droplet rain, kg s^{-1} m^{-2}

683 Nu Nusselt number ($Nu = U\,d\,/\,k$), dimensionless

684 n exponent in ice deformation equation (Equation 22), dimensionless

685 P pressure, Pa

686 p partial pressure of the absorbing gas in the layer, Pa

687 pL optical depth, Pa m

688 Pr Prandtl number ($Pr = \mu\,C_p / k$), dimensionless

689 Q heat flux to ice surface, W m^{-2}

690 Q_r net radiation to droplet surface, W m^{-2}

691 q heat transfer rate per unit length, W m^{-1}

692 R cavity radius, m

693 Re Reynolds number ($Re = u_t\,\rho_g\,d\,/\,\mu$), dimensionless

694 T_d droplet surface temperature, K

695 T_g gas temperature, K

696 T_i ice temperature, K

697 T_L temperature of eruption jet surface, K

698 T_s temperature of radiating surface, K

699 U heat transfer coefficient, W m^{-2} K^{-1}

700 u velocity, m s^{-1}

701 u_t average droplet terminal velocity, m s^{-1}

702 α_g absorbtivity of a gas, dimensionless

703 ΔH vertical height of finite element, m

704 ΔP pressure difference, Pa

705 ΔP_a cavity underpressure, Pa

706 ΔP_d pressure difference for downward flow, Pa

707 ΔP_i pressure difference over vertical element, Pa

708 ΔP_{dr} “driving” pressure difference, Pa

709 ΔP_r pressure difference in upward flow, Pa

710 ΔP_{res} “resisting” pressure difference, Pa

711 Δq total heat removal rate per unit length for an element, W m^{-1}

712 ΔT_g temperature change of steam, K

713 δ liquid film thickness, m

714 ε_g gas emissivity, dimensionless

715 κ attenuation coefficient, m^{-1}

716 μ viscosity of steam, Pa s

717 φ absorption coefficient, Pa^{-1} m^{-1}

718 ρ density, kg m^{-3}

719 ρ_{dr} droplet density, kg m^{-3}

720 ρ_i steam density, kg m^{-3}

721 ρ_w liquid water density, kg m^{-3}

722 ρ_1 density at top of upward flow, kg m^{-3}

723 ρ_2 density at bottom of upward flow, kg m^{-3}

724 σ Stefan-Boltzmann constant, W m^{-2} K^{-4}

725 τ_g shear stress on liquid film surface, Pa

726 θ inclination of surface from horizontal, degree

727

Acknowledgements

The data supporting this paper are available as Supporting Information. We sincerely thank Magnus Tumi Gudmundsson, John Stevenson and an anonymous reviewer for their detailed comments during review which have greatly improved the paper. We also thank the Editor André Revil and the Associate Editor for their comments. We are grateful to Lionel Wilson for comments on an early version of this paper.

References

Brandl, R. E., and S. G. Warren (1993), Solar-heating rates and temperature profiles in Antarctic snow and ice, *J. Glaciol., 39*, 99-110.

Cheng, X., and U. Muller (1998), Turbulent natural convection coupled with thermal radiation in large vertical channels with asymmetric heating, *Int. J. Heat Mass Transfer*, *41*, 1681-1692.

Davies, G. D., L. Keszthelyi, and A. S. McEwen (2011), Estimating eruption temperature from thermal emission spectra of lava fountain activity in the Erta'Ale (Ethiopia) volcano lava lake: Implications for observing Io's volcanoes, *Geophys. Res. Lett.*, *38*, L21308.

Gudmundsson, M. T. (2005), Subglacial volcanic activity in Iceland, in *Iceland: Modern processes, Past Environments, Developments in Quaternary Science,* vol. 5*,* edited by C. J. Caseldine et al., pp. 127-151, Elsevier, Amsterdam.

753 Gudmundsson, M. T., F. Sigmundsson, H. Bjornsson, and T. Hognadottir (2004), The
754 1996 eruption at Gjálp, Vatnajökull ice cap, Iceland: efficiency of heat transfer, ice
755 deformation and subglacial water pressure, *Bull. Volcanol., 66*, 46-65.
756
757 Hobbs, P. V. (1974), *Ice Physics*, Clarendon Press, Oxford.
758
759 Höskuldsson, A., and R. S. J. Sparks (1997), Thermodynamics and fluid dynamics of
760 effusive subglacial eruptions, *Bull.Volcanol., 59*, 219-230.
761
762 Hottel, H. C., and A. F. Sarofim (1967), *Radiative heat transfer*, McGraw Hill, New
763 York.
764
765 Incropera, F. P., and D. P. DeWitt (1996), *Introduction to heat transfer,* John Wiley,
766 New York.
767
768 Li, R., M. Bousetta, E. Chenier, and G. Lauriat (2013), Effect of surface radiation on
769 natural convective flows and the onset of flow reversal in asymmetrically heated
770 vertical channels, *Int. J. Therm. Sci., 65*, 9-27.
771
772 Magnússon, E., M. T. Gudmundsson, G. Sigurdsson, M. J. Roberts, F. Höskuldsson,
773 and B. Oddsson (2012), Ice-volcano interactions during the 2010 Eyjafjallajökull
774 eruption, as revealed by airborne radar, *J. Geophys. Res.*, *117*, B07405,
775 doi:10.1029/2012JB009250.
776
777 Massey, B. S. (1970), *Mechanics of fluids*, Van Nostrand Reinhold, London.

Major, J.J. and C.G. Newhall (1989), Snow and ice perturbation during historical volcanic eruptions and the formation of lahars and floods, *Bull.Volcanol., 52*, 1-27.

Pinkerton, H., M. James, and A. Jones (2002), Surface temperature measurements of active lava flows on Kilauea volcano, Hawaii. *J. Volcanol. Geotherm. Res., 113,* 159-176.

Ranz, W. E., and W. R. Marshall (1952), Evaporation from drops, *Chem. Eng. Prog., 48,* 141-146.

Rohsenow, W. M., J. H. Webber, and A. T. Ling (1956), Effect of vapor velocity on laminar and turbulent film condensation, *Trans. ASME, 78*, 1637-1643.

Spampinato, L., S. Calvari, C. Oppenheimer, and L. Lodato (2008), Shallow magma transport for the 2002-3 Mt. Etna eruption inferred from thermal infrared surveys. *J. Volcanol. Geotherm. Res., 177,* 301-312.

Tuffen, H. (2007), Models of ice melting and edifice growth at the onset of subglacial basaltic eruptions, *J. Geophys. Res., 112*, B03203, doi:10.1029/2006JB004523.

Vergniolle, S., and M. Mangan (2000), Hawaiian and strombolian eruptions, in: *Encyclopaedia of Volcanoes*, edited by H. Sigurdsson, pp. 447–461, Academic Press, San Diego.

Wilson, L., J. L. Smellie and J. W. Head (2013), Volcano-ice interactions, in *Modelling Volcanic Processes*, edited by S. A. Fagents et al., pp 275-299, Cambridge University Press.

Woodcock, D. C., S. J. Lane, and J. S. Gilbert (2014), Ice-melt rates in liquid-filled cavities during explosive subglacial eruptions, *J. Geophys. Res. Solid Earth, 119*, doi:10.1002/2013JB010617.

Woodcock, D. C., J. S. Gilbert, and S. J. Lane (2015), Ice-melt rates by steam condensation during explosive subglacial eruptions, *J. Geophys. Res. Solid Earth, 120,* doi:10.1002/2014JB011619.

YouTube (2007), The Eruption of Kilauea 1959-1960 Chap 3 – YouTube. https://www.youtube.com/watch?v=aa8Wr6xZPYI (accessed 14 January 2016).

820 **Figures with captions**

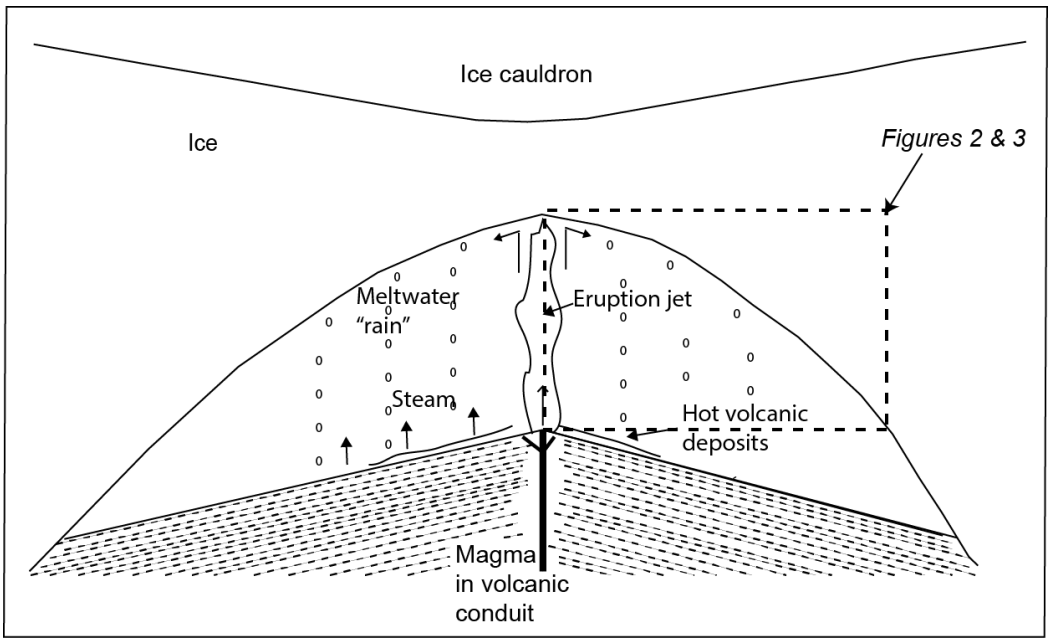

821

822 **Figure 1**. Schematic diagram of an ice cavity formed during a subglacial fissure
823 eruption which has drained and depressurized to allow the formation of an eruption
824 jet. In general, steam is produced by magma-water interaction within the volcanic
825 conduit and by contact of the meltwater rain with hot volcanic deposits on either side
826 of the eruption jet. The dashed rectangle indicates the location of Figures 2 and 3.

827

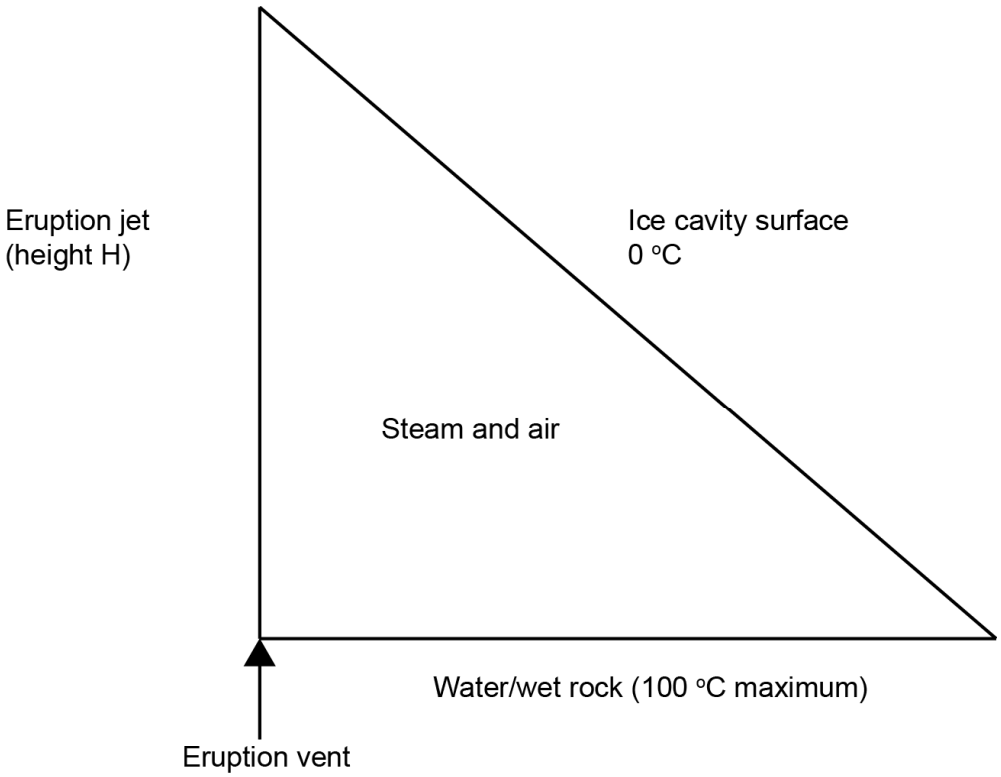

828

829 **Figure 2**. Conceptual model for radiative heat transfer from a linear, dyke-fed
830 eruption jet in a subglacial cavity at atmospheric pressure. The cavity is assumed
831 symmetrical about a center line above the eruption vent and the diagram shows the
832 right hand side of the cavity only.

833

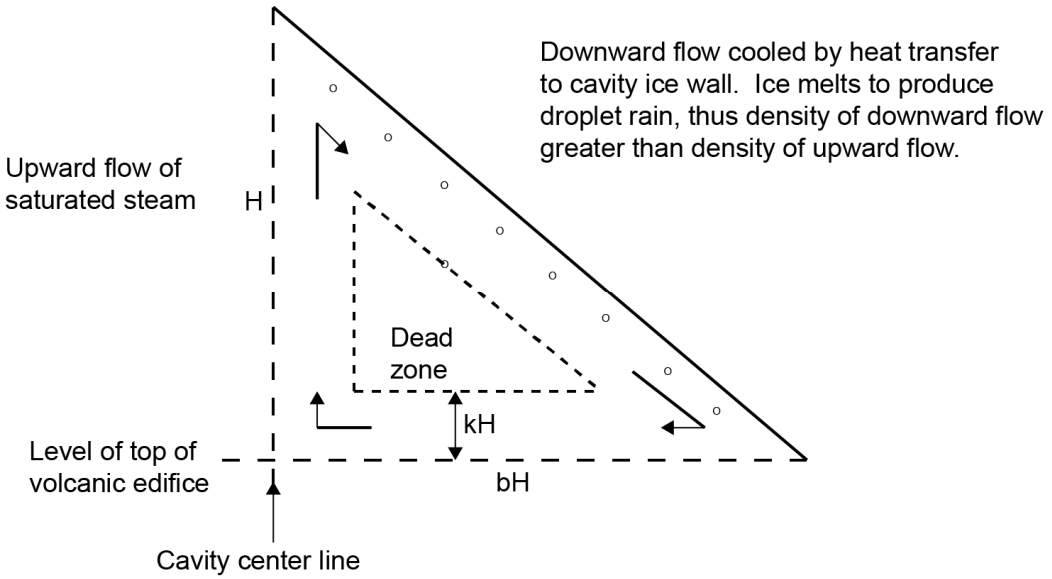

834

835 **Figure 3.** Free convective heat transfer and ice melting in a model subglacial eruption
836 cavity. The cavity is symmetrical about the centre line, and the right hand half of the
837 cavity only is shown. The third dimension (length) extends into the paper with the
838 model developed for unit length.

839

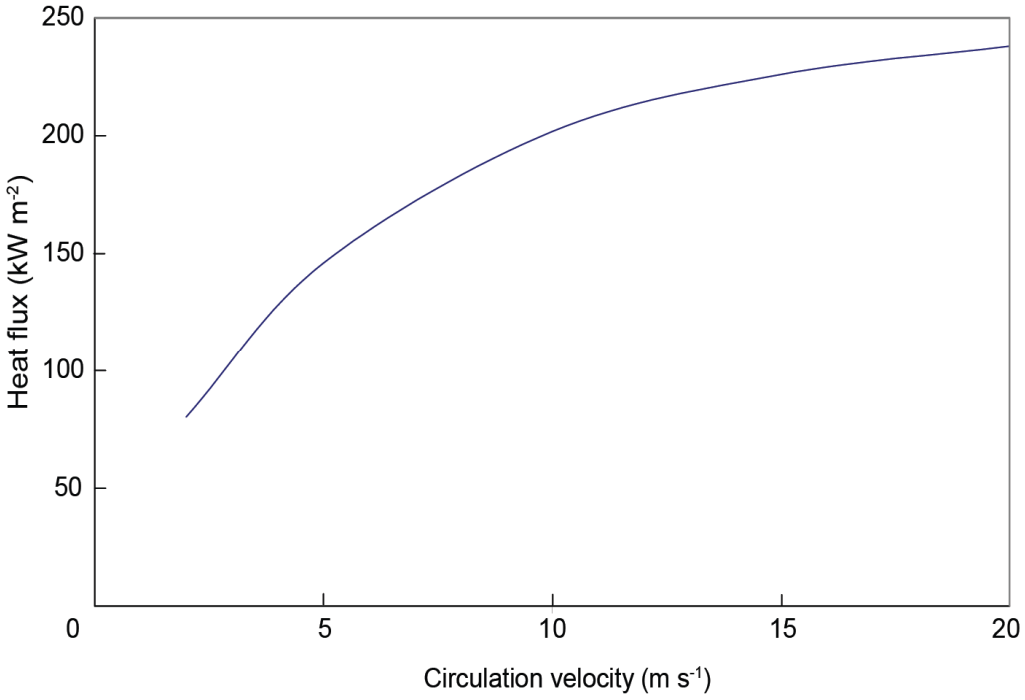

840

841 **Figure 4**. Variation of condensing heat flux with circulation velocity for a subglacial

842 cavity at 0.1 MPa, with condensation from saturated vapour at 373 K. For the range

843 of velocities encountered on Table 1 the heat flux varies by approximately 20%.

844

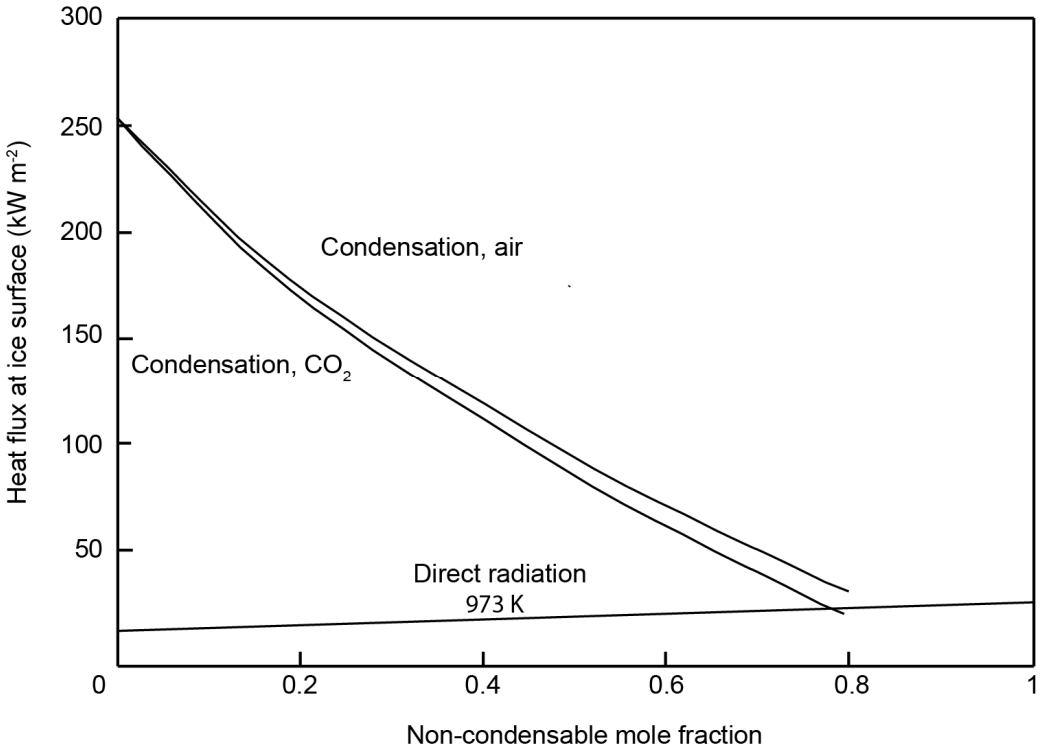

845

846 **Figure 5.** Variation of heat flux on the ice cavity surface with mole fraction and
847 nature of the non-condensable component. Two curves are shown for the condensation
848 heat flux during radiatively-enhanced free convection for an eruption jet temperature
849 of 973 K: one for air (which is assumed to be radiatively transparent) and one for CO_2
850 (with radiative properties of steam). A third solid line shows schematically the likely
851 variation in direct radiative heat flux at 973 K. The total heat flux is the sum of the
852 condensation and direct radiative heat fluxes.

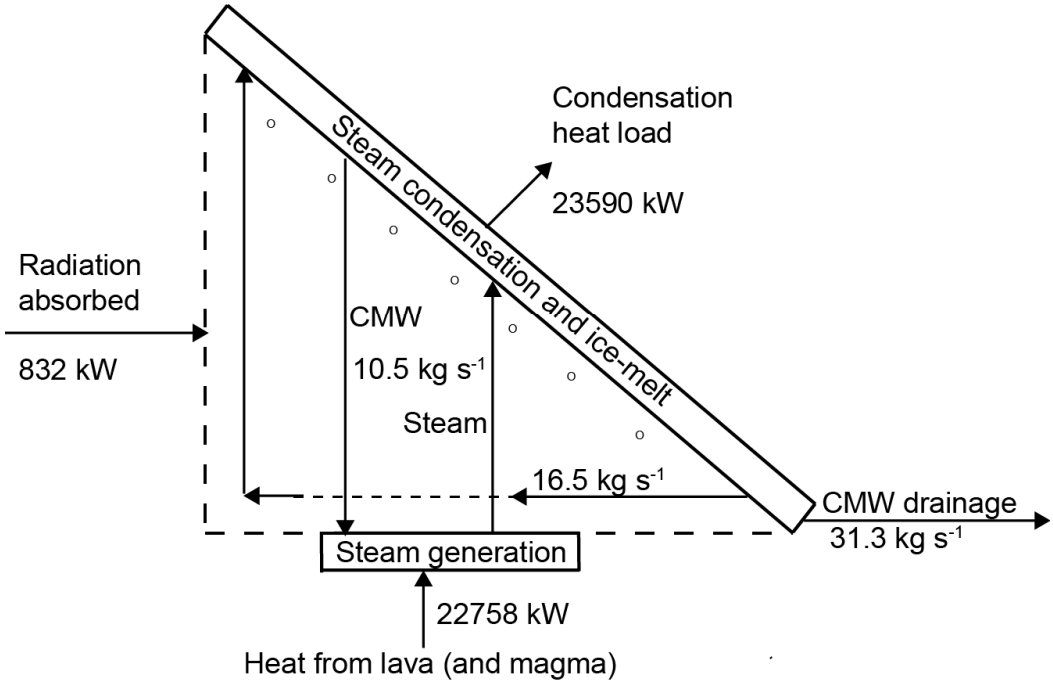

853

854 **Figure 6.** Block diagram of the overall mass and heat balance for the convection

855 system within the ice cavity for the reference case in Table 1. Flowrates are for unit

856 length of fissure. CMW = condensate plus meltwater.

857

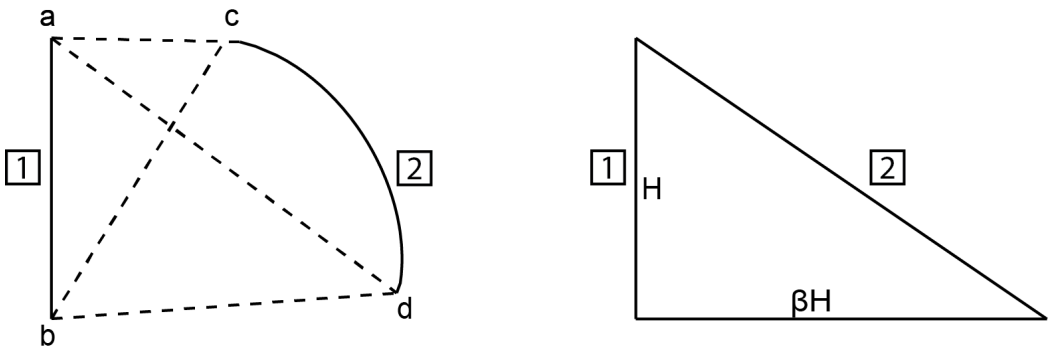

$$F12 = \frac{(ad + bc) - (ac + bd)}{2ab}$$

$$F12 = \frac{(H\,(1 + \beta^2)^{1/2} + H) - (0 + \beta H)}{2H}$$

$$= \frac{(1 + \beta^2)^{1/2} + (1 - \beta)}{2}$$

858

859

860 **Figure A1.** The diagram on the left hand side shows the general version of Hottel's

861 "crossed string" rule [*Hottel and Sarofin*, 1967], in which notional strings are attached

862 to the ends of the two surfaces (labeled 1 and 2) as shown by the dashed lines. The

863 formula for the view factor involves the difference between the sum of the crossed

864 strings and the sum of the uncrossed strings. The diagram on the right hand side

865 applies the rule to the geometry of the subglacial cavity (with height H). If $\beta = 1$, the

866 value of F_{12} is $1/\sqrt{2}$.

867

868

Tables

Table 1. Sensitivity of model results to changes in input variables (names of variables changed and value of variable changed are in italics). The non condensable mole fraction is 0.1.

Variable	Case							
	Reference	2	3	4	5	6	7	8
Cavity height, H (m)	50	*100*	50	50	50	50	50	50
Cavity aspect ratio, b	2	2	*4*	2	2	2	2	2
Flow area fraction, k	0.05	0.05	0.05	*0.1*	0.05	0.05	0.05	0.05
Bend loss coefficients, K[a]	1	1	1	1	*2*	1	1	1
Jet temperature[b] *(K)*	973	973	973	973	973	*773*	*370*	973
Cavity fluid pressure (MPa)	0.1	0.1	0.1	0.1	0.1	0.1	0.1	*0.2*
Top[c] steam temperature (K)	394	389	395	385	403	380	370	405
Top steam velocity (m s^{-1})	11.2	16.2	10.9	10.3	8.3	9.8	8.6	10.4
Circulation rate (kg s^{-1} m^{-1})	16.5	48.3	16.0	31.1	12.0	15.0	13.5	30.0
Heat flux (kW m^{-2})	211	243	209	203	204	199	186	315

[a]Factor relative to reference case.

[b]Mean radiant temperature of pyroclast surfaces.

[c]Top of upward flow.